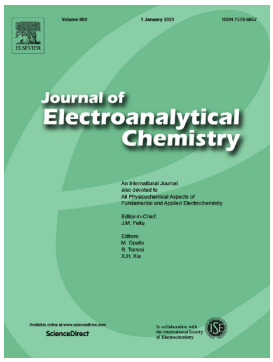

Synergistic effect on electrochemical performance of LiFePO4 cathodes via carbon coating and Ni2+ doping: a combined experimental and theoretical approach

Shreyas J. Kashyap, Ch. Gowthami, Sougat Purohit, Gopalakrishnan Sai Gautam, Vadali V.S.S. Srikanth, R. Vijay, Tata N. Rao, S. Anandan

PII: S1572-6657(25)00497-7

DOI: https://doi.org/10.1016/j.jelechem.2025.119423

Reference: JEAC 119423

To appear in: *Journal of Electroanalytical Chemistry*

Received date: 24 June 2025

Revised date: 11 August 2025

Accepted date: 18 August 2025

Please cite this article as: S.J. Kashyap, C. Gowthami, S. Purohit, et al., Synergistic effect on electrochemical performance of LiFePO4 cathodes via carbon coating and Ni2+ doping: a combined experimental and theoretical approach, *Journal of Electroanalytical Chemistry* (2024), https://doi.org/10.1016/j.jelechem.2025.119423

Synergistic effect on electrochemical performance of $LiFePO_4$ Cathodes *via* carbon coating and Ni^{2+} Doping: A Combined Experimental and Theoretical Approach

Shreyas J. Kashyap[a, b], Ch. Gowthami[a], Sougat Purohit[c], Gopalakrishnan Sai Gautam[c]
Vadali V S S Srikanth[b], R. Vijay[a], Tata N. Rao[d], S. Anandan[a, *]

[a] *Centre for Nanomaterials, International Advanced Centre for Powder Metallurgy and New Materials (ARCI), Balapur, Hyderabad 500005, Telangana, India*

[b] *School of Engineering Sciences and Technology, University of Hyderabad, Hyderabad 500046, Telangana, India*

[c] *Department of Materials Engineering, Indian Institute of Science, Bengaluru, Karnataka 560012, India*

[d] *Department of Materials Science & Metallurgical Engineering, Indian Institute of Technology, Hyderabad 502285, India*

**Corresponding author e-mail: anandan@arci.res.in*

Abstract

The development of high-power cathode materials is critical for meeting the growing demand for high-rate performance in lithium-ion batteries (LIBs) used in portable electronics, electric vehicles, and grid storage. In this work, an ultra high-rate-performance $LiFePO_4$ (LFP) cathode material is synthesized through a synergistic strategy combining Ni^{2+}-ion doping, uniform carbon coating, and particle size reduction. Structural analysis by XRD confirms the orthorhombic phase of LFP, while FE-SEM images reveal pulverized particles in the 1-10 μm, and HR-TEM confirms homogeneous carbon coating. Rietveld refinement shows that Ni^{2+} doping reduces cell volume and lattice parameters, altering the Li-ion local environment, as further supported by density functional theory calculations. XPS analysis confirms the presence of Fe exclusively in the Fe^{2+} state. Electrochemical performance demonstrated outstanding performance with a high discharge capacity of 171 mAh g^{-1} at C/5 rate, remarkable rate capability of 136 mAh g^{-1} at 10C with a flat 3.3 V plateau, and over 80% capacity retention after 200 cycles at 5C. The exceptional performance is attributed to reduced particle size, improved electrode kinetics from Ni^{2+} doping, and an enhanced Li-ion transport. These findings position Ni-LFP/C as a promising high-power cathode material for next generation LIB applications for high-power LIB applications.

Keywords: Cathode material, Li-ion battery, Ni^{2+} doping $LiFePO_4$, olivine-type, ball milling.

1. Introduction

The olivine-type lithium iron phosphate $LiFePO_4$ (LFP) is one of the cathode materials being employed for Li-ion batteries (LIB) due to several advantages such as low raw material cost, environmental benignity, high structural and thermal stability and long cycle life. In addition to this, LFP displays a stable constant voltage curve at 3.45 V (*vs.* Li/Li^+) along with appreciable specific capacity of 170 mAh g^{-1} [1–3]. The LFP cathode material adopts an olivine structure adopting *Pnma* space group. Each unit cell consists of one lithium (Li), iron (Fe), and phosphorus (P) atom, along with four oxygen (O) atoms. In typical $LiFePO_4$ structure, each iron (Fe) atom is surrounded by an oxygen octahedron. This means that there are six oxygen atoms forming an octahedral shape around each iron atom (FeO_6). The phosphate (PO_4) groups are situated between the iron-oxygen octahedra, and the phosphorus atom (P) residing at the center bonded with four oxygen atoms. Lithium atoms are located within channels formed by the phosphate groups. These channels run along one direction [010] within the crystal lattice [4,5]. However, LFP exhibits low electronic conductivity because the structure lacks a continuous network of FeO_6 octahedra since it is blocked by the PO_4 tetrahedron [6,7]. In addition, the poor Li^+ diffusivity arises from the fact that LFP accommodates only one-dimensional Li^+ diffusion pathway i.e., Li^+ moves only in the channels parallel to [010] [8,9].

To address these challenges, several key approaches are identified and put forward: one, surface coating of LFP particles with conductive carbon can improve the material electrical conductivity [10,11]; two, nano-structuring, which reduces the Li^+ diffusion pathway thereby improving the ion diffusion [12–14] and three, substitution or doping of certain metal ions into the LFP crystal structure [15–17]. Metal ion insertion, either into the Li or Fe-site can enhance the diffusivity of Li^+ as well as increase the intrinsic electronic conductivity. It is believed that multi-ion doping enhances the Li^+ diffusion kinetics during charging and discharging, and also widens the Li^+ diffusion channels in the crystal structure [18,19]. Carbon-coating, Fe-site substitution, and nano-structuring have proven to be highly effective methods in addressing the limitations of $LiFePO_4$ cathode material. The incorporation of certain metal-cations through doping is widely accepted and often adopted for enhancing the electrochemical performance of $LiFePO_4$ [20,21]. Notable improvements in the electrochemical performance of doped $LiFePO_4$, particularly at very low concentrations of the dopant have been confirmed in previous studies. For instance, Liu et al [22] demonstrated that $LiFePO_4$/C showed an enhancement in electron conductivity by 275 times after Mg^{2+} doping. The doped material exhibited a higher discharge capacity (155 mAh g^{-1} vs. 144.6 mAh g^{-1} for pristine LFP at 0.5C) and an

approximately 3.6-fold increase in the Li^+ diffusion coefficient compared to pure LFP. The authors explained this by citing shortened Fe-O and P-O bonds and lengthened Li-O bonds, which widened the pathways for Li^+ diffusion channels. Teng et al [23] reported that Nb^{5+} doped $LiFePO_4$ (LiFNbPO-0.75) showed discharge capacity of 169.87 mAh g^{-1} for the initial cycle at C/10, and it was able to retain its capacity for up to 99% after 100 cycles. It was argued that doping with Nb^{5+} resulted in the widening of the crystal plane space and also led to low charge transfer impedance. Jian and Wang [24] showed that nanosized vanadium-doped $LiFePO_4$ exhibited a specific capacity of 142.7 mAh g^{-1} after 200 cycles, measured at10C current rate. They observed a capacity of 162.9 mAh g^{-1} demonstrated at C/10, although the cost of dopant seems to be expensive.

Despite notable advancements, significant challenges remain in developing $LiFePO_4$ based cathode materials that simultaneously deliver high power, high specific capacity, and long-term cyclic stability. Key obstacles include achieving uniform and optimally thin carbon coatings, minimizing defects and impurities introduced by metal-ion doping, simplifying often complex multi-step synthesis processes, and addressing the high cost of certain dopant precursors such as V, Ti, Zr, and Nb. Additionally, developing facile, scalable, and cost-effective methods for producing nanosized $LiFePO_4$/C particles remains critical. Recognizing that nickel (Ni^{2+}) precursors are relatively inexpensive compared to other commonly studied dopants and that Ni^{2+}-doped $LiFePO_4$/C remains underexplored, we adopted a synergistic approach to synthesize a high capacity cathode material via: (i) doping a small concentration of Ni^{2+} ions at the Fe^{2+} sites using a solid-state milling approach, (ii) achieving particle size reduction, and (iii) generating a homogenous, thin carbon coating on the $LiFePO_4$ surface. The resulting Ni-doped $LiFePO_4$/C (Ni-LFP/C) material was extensively characterized by adopting both experimental and computational methods to understand the effects of Ni doping. Our analysis shows that the particle shape and particle size of Ni-LFP/C are retained even after doping. This integrated approach resulted in a high-performance electrode, delivering an appreciable capacity of 171 mAh g^{-1} at C/5, superior rate performance (136 mAh g^{-1} @10C), in addition to outstanding cyclic stability with retention of 80%, noted at 5C after 200 cycles. These exceptional electrochemical properties underscore the potential of Ni-doped $LiFePO_4$/C as a superior cathode electrode material for the fabrication of high-power Li-ion battery. Moreover, the synergistic strategy demonstrated here could be extended to other cathode and anode systems, contributing to the development of next-generation high-rate energy storage technologies.

2. Experimental section

A simple ball milling route has been employed to synthesize $LiFePO_4$/C. It was prepared by milling Li_2CO_3 (99%, SRL), $FeC_2O_4 \cdot 2H_2O$ (99%, Aldrich) and $NH_4H_2PO_4$ (98-101%, Fisher Scientific) in ethanol, using a planetary mill (pulverisette 5, FRITSCH). In addition, citric acid (99%, SRL) was used as the precursor for carbon coating and as a complexing agent to avoid Fe oxidation from +2 to +3 while calcining the milled material. For the doped sample Ni^{2+}-doped $LiFePO_4$, $(CH_3COO)_2Ni \cdot 4H_2O$ (98%, LOBA Chemie) was used as the precursor for Ni doping. Ni-doped LFP has been synthesized by taking Li, Fe, Ni, and P in the stochiometric molar ratio of 1:0.99:0.01:1 respectively ($LiFe_{0.99}Ni_{0.01}PO_4$/C). For planetary ball milling, stainless steel (SS) vials were used with SS balls having diameter 3 mm as grinding media with the powder to ball ratio maintained at 1:10. For the synthesis of Ni doped LFP, all the precursors including Ni dopant were dispersed into acetone and milled at 250 rpm with the milling time and rest time of 10 and 5 min, respectively for 21 repetitions. Similarly, $LiFePO_4$/C has been milled without addition of Ni source. Further, the milled powders were then dried overnight at 80 ℃ to evaporate the solvent and finally pelletized and heated to 750 ℃ for 12 h in a tube furnace. The heating rate was maintained at 5 ℃ min^{-1} and Ar gas was continuously purged during heating and natural cooling. As synthesized samples, $LiFePO_4$/C and Ni^{2+}-doped $LiFePO_4$ were designated as LFP/C and Ni-LFP/C, respectively.

2.1 Materials characterization

Morphological features of the developed materials were checked through Gemini 500, Carl Zeiss field emission scanning electron microscope (FE-SEM) operated at a voltage of 5 kV. For analyzing bulk chemical composition, energy dispersive X-ray spectroscopy (EDS) studies were carried out using an attached EDS unit (AMETEK, octane) to the FESEM. For TEM imaging, ethanol-dispersed samples were drop-casted onto a lacey carbon-coated Cu grid and left for solvent evaporation. The TEM images, scanning TEM (STEM), and EDS spectra and maps were obtained by employing a Jeol JEM F200 Multipurpose electron microscopy operating at 200 kV. Gatan One view camera was used to acquire TEM images. Powder X-ray diffraction experiment (XRPD) was performed using Rigaku SmartLab high-flux XRD with 45 kV working voltage and filament current of 200 mA. XRPD patterns were measured in the 2θ range of 10-100° at room temperature. The automated multipurpose XRPD was equipped

with a 9-kW rotating anode (Cu K_α; λ=1.54 Å) and D/tex Ultra 250 detector having a parabolic multilayer X-ray mirror with cross beam optics. The patterns were matched using MATCH Software which employed the ICDD PDF-4+ 2022 database. For pattern refinement, general structural analysis software II (GSAS-II) was used with the Rietveld method of refinement. The patterns were refined using an orthorhombic $Pnma$ (No. 62) standard (ICDD #04-015-6173). The background correction was carried out using a Chebyshev polynomial function with up to 12 background coefficients. The reliable fits (the fits for which the Rietveld refinement R value, namely the R_{wp} and the goodness-of-fit (GoF) are close to desirable values) are only considered for analysis. N_2 physisorption isotherms were performed employing a Quantatchrome surface area analyzer. Sample degassing was carried out at 140 ℃ for 5 h before analysis. The BET isotherm equation was used for calculating the specific surface area and the DFT method was used for deriving total pore volume. Raman analysis was carried out using a Raman spectrometer from WiTec having a green laser (532 nm). Elemental oxidation states were studied through X-ray photoelectron spectroscopy using a Thermo Fischer Scientifc which uses an Al K_α radiation. A Carbon-Sulphur analyzer (CS-444, Leco, USA) was employed for measuring the amount of carbon (wt%) in the synthesized samples. Chemical analysis of Li, Fe, P and Ni was examined through Inductively coupled plasma spectroscopy (ICP-OES, Agilent 5110). Before analysis, approximately 100 mg of the sample was digested in a 1:3 mixture of HNO_3 and HCl, and used for the measurement. Thermogravimetric analysis (TGA) of synthesized materials were tested at a temperature range of 30℃ to 800℃, and under heating rate of 10°C/min in air atmosphere.

2.2 Electrochemical characterization

Electrode sheets were coated by mixing (in wt%) 80% cathode active material, 10% carbon conductive agent (CNT-multiwalled, TCI C2154, 20-40 mm diam., 5-15 μm length) and 10% polymeric binder (polyvinylidene fluoride, pvdf, Solef® 5130/1001 Solvay) using NMP solvent (n-methyl 2-pyrollideine, 98%, LOBA Chemie) thoroughly and finally coating the wet slurry on a carbon-coated aluminum current collector (18 μm, GELON LIB group) using a doctor blade set-up (AFA-III automatic thick film coater, MTI Corp.). Before wet-slurry mixing, synthesized materials were mixed with CNT and then ball milled for a period of 2 h in a desk-top planetary ball miller (SFM-1, MTI Corp.) using ceramic vials using 3 mm ZrO_2 balls (ball:powder=20:1). The wet thickness was set to 150 μm resulting in an mass loading of 1.5

mg cm^{-2} for working electrode, after drying at 80 ℃ overnight and roll pressing (hot roll press GN-MR-200H). Electrochemical validation of material was carried out using swagelok-type half-cell assembly. Li-foil was employed as a counter electrode, where GF/D glass fiber (GE healthcare) was used as the separator which was soaked with 1M $LiPF_6$ (EC:DMC in 1:1 vol%, with 2% VC) electrolyte as additive. All cells were assembled inside an Ar glovebox (Mbruan unilab pro SP), where H_2O and O_2 were maintained below 0.1 ppm.

Cyclic voltammetry (CV) experiments were demonstrated at a scan rate of 0.1 to 0.5 mV s^{-1}, between the voltage limits of 2.0-4.2 V (*vs* Li/Li^+) and electrochemical impedance spectroscopy (EIS) was done under the limits of 10^{-2} Hz $\leq f \leq 10^6$ Hz with a sinusoidal amplitude of 10 mV. Here, CV and EIS experiments were done using PARSTAT MC2000 electrochemical workstation. Further, the constant-current/galvanostatic experiments (2.0-4.2 V) were performed to evaluate the rate performance and cycling stability of coated electrodes at different C-rates using Arbin instruments (BT2000). Here, C/n is the calculated current density which is needed to completely discharge or charge a cell in n h . For example, a C-rate of C/10 or 5C means that the cell is fully charged or discharged in n =10 h or n =1/5 h, respectively. For the long cycling experiments, the cells were cycled at C/10 thrice before stepping up the current rate to 1C or 5C. More importantly, active material mass was considered to calculate the specific charge/discharge capacities. All the electrochemical measurements were conducted at 28±1 ℃.

We performed density functional theory (DFT) [25] calculations on the LFP and Ni-doped LFP using the Vienna ab initio simulation package (VASP) [26–28]. We utilized plane-wave basis sets (with a cut-off energy of 520 eV), projected augmented wave (PAW) [29] potentials and the Hubbard *U* corrected [30,31] strongly constrained and appropriately normed (SCAN) [32] exchange-correlation functional. We started with the experimental olivine LFP structure, as available in the inorganic crystal structure database [33] and relaxed its atomic positions, cell shape, and cell volume without preserving any symmetry. Subsequently, we constructed a 2×2×1 supercell (ensuring all lattice parameters are above 9 Å in length) of the relaxed LFP and randomly substituted one of the Fe sites with a Ni and relaxed the atomic positions only of the substituted structure. All structure relaxations were performed with an energy convergence criterion of 10^{-5} eV, and an atomic force convergence criterion of |0.03| eV $Å^{-1}$. Finally we performed the density of states (DOS) calculations on the relaxed Ni-LFP and a 2×2×1

supercell of relaxed pristine-LFP using an energy convergence criterion of 10^{-6} eV. All the structure relaxations and DOS calculations were performed using Γ-centred *k*-points with a mesh density of 48 $Å^{-1}$, and Hubbard *U* corrections of 3.1 for Fe and 2.5 for Ni [34,35].

3. Results and Discussions

XRD profiles of synthesized pristine and doped carbon coated LFP (Fig. 1a) were indexed to orthorhombic structure with space group *Pnma* #62. Also, the diffraction peaks in the case of both LFP/C and Ni-LFP/C cathode materials align with the standard data (ICDD #04-015-6173) of $LiFePO_4$. Further, no other crystalline phases have been observed, implying that the ball-milling method combined with carbothermal reduction is apt for preparing phase pure (orthorhombic) LFP/C and Ni-LFP/C samples. Presence of controlled inert working (Ar gas flow) atmosphere during calcination and the carbon coating that creates reducing atmosphere, helps in preventing the formation of possible impurities such as $Li_3Fe_2PO_4$, $LiFeP_2O_7$, Fe_2O_3, Fe_2P etc.

Table 1 Crystallographic lattice and Rietveld refinement parameters for the synthesized samples

	$LiFePO_4$/C	Ni-$LiFePO_4$/C
Crystal structure	Orthorhombic	Orthorhombic
Space group	*Pnma* (No. 62)	*Pnma* (No. 62)
$\boldsymbol{a}$ (Å)	10.33(4)	10.32(4)
$\boldsymbol{b}$ (Å)	6.01(20)	6.00(19)
$\boldsymbol{c}$ (Å)	4.70(16)	4.69(18)
$\boldsymbol{V}$ ($Å^3$)	292.19(13)	291.47(11)
$\boldsymbol{\alpha = \beta = \gamma}$ (°)	90	90
Average Li-O (Å)	2.07	2.16
Average Fe-O (Å)	2.22	2.15
Average P-O (Å)	1.56	1.54
$\boldsymbol{Z}$	4	4
$\boldsymbol{R_{wp}}$ (%)	1.489	1.400
GoF (%)	2.43	2.22

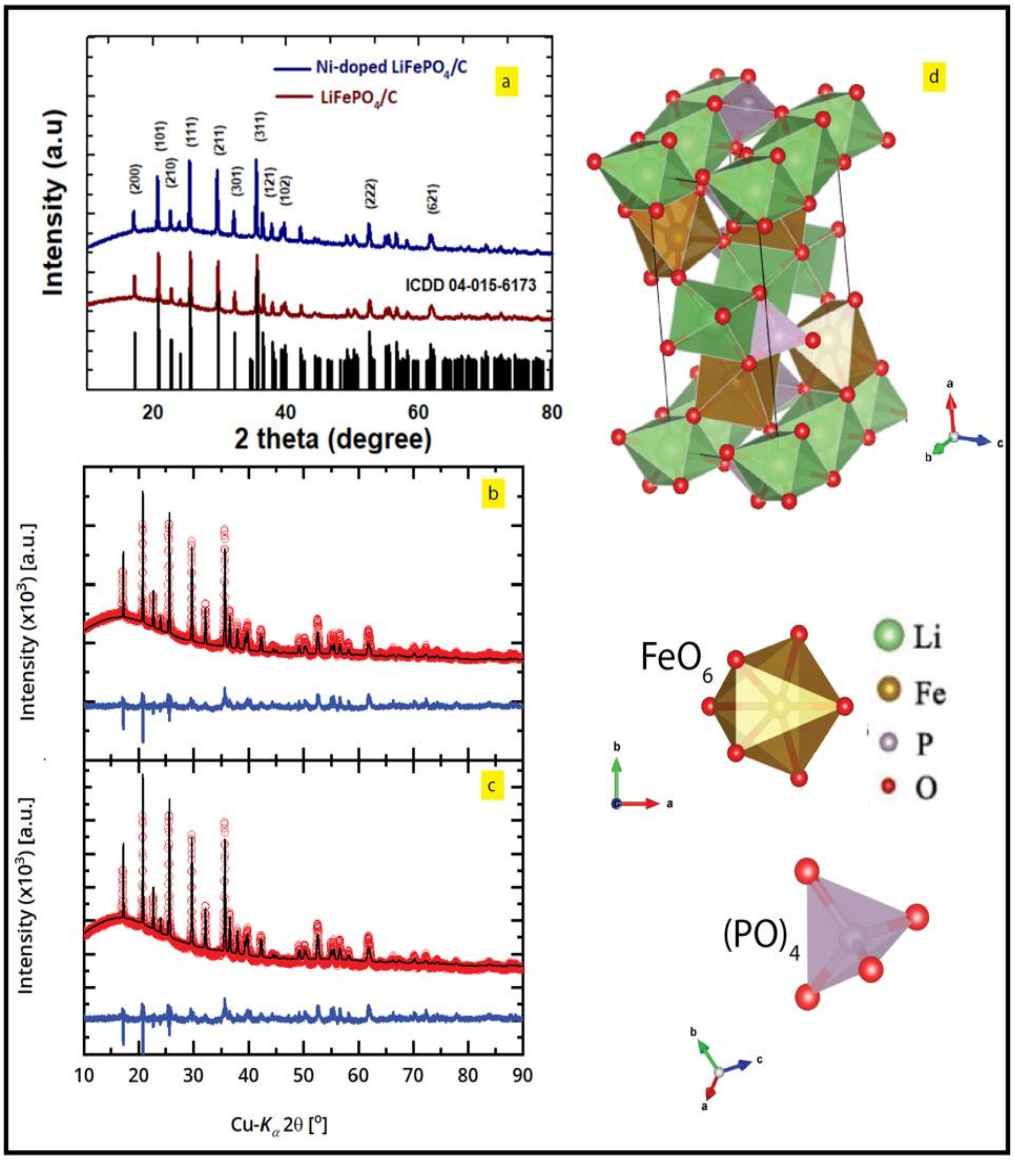

Fig. 1 XRD patterns (a) Rietveld refinement (b, c) of $LiFePO_4$/C and Ni-doped $LiFePO_4$/C; refined crystal structure of carbon-coated Ni^{2+} doped $LiFePO_4$ prepared in this study (d)

Moreover, no extra diffraction peaks associated with carbon or Ni^{2+} doping are observed, suggesting that carbon in LFP/C and Ni-LFP/C is amorphous [36], and the amount of Ni^{2+} in Ni-LFP/C is be fractional. Rietveld refinements are conducted on the XRD patterns (Fig. 1(b, c)), and the corresponding results are tabulated as shown in Table 1, and the crystal structure of LFP has been shown in Fig. 1(d). The cell volumes of LFP/C and Ni-LFP/C from Rietveld refinements are found to be 292.19(13) Å and 291.47(11) Å, respectively. Similarly, the lattice constants a, b and c for LFP/C and Ni-LFP/C are found to be 10.336, 6.014, 4.70 and 10.327, 6.008, 4.698 Å, respectively. It can be observed that the lattice parameters have reduced after

incorporation of Ni^{2+}. The doping of Ni^{2+} in the $LiFePO_4$ crystal structure can be ascribed to the small radius of Ni^{2+} (r = 69 pm), than Fe^{2+} (r = 74 pm) [37]. This size difference resulted in the reduction of Ni-doped $LiFePO_4$/C lattice parameters, which is supported by the Rietveld 'R' values and the observed lowering in the lattice parameters (Table 1). Furthermore, the bond length averages of P-O and Fe-O reduced when Ni^{2+} is doped into LFP unit cell, whereas it increased for Li-O bonds. This adjustment in bond lengths also results in the broadening of the Li-ion diffusion path i.e., in the [010] direction of the $LiFePO_4$ crystal structure [38] due to Ni^{2+} doping on Fe^{2+} site of LFP. Overall, XRD, and Rietveld refinement revealed the formation of pure LFP phase without any impure phases.

From the FE-SEM micrographs captured at lower and higher magnification as shown in Fig. 2(a-f) depicts insignificant morphological changes for both LFP/C and Ni-LFP/C samples. Similar conclusions can also be drawn regarding particle size for both pristine and doped LFP. Pristine and doped LFP samples have particle sizes around 1 μm and show pulverized and irregular spherical morphology. However, less agglomerated particles are observed for Ni-LFP/C than for pristine LFP/C. Aggregation of particles leading to tortuous travel path for e^- and Li^+-ions results in poor kinetics for LFP/C. The reduction in agglomeration observed upon Ni doping can be attributed to the influence of Ni^{2+} ions on the crystal growth kinetics and surface energy during synthesis. Specifically, the incorporation of Ni^{2+} into the LFP lattice modifies the local bonding environment and alters the surface energy of growing crystallites [39].This change can inhibit uncontrolled particle growth and reduce the tendency of primary particles to fuse during high-temperature calcination.

Moreover, Ni doping may introduce slight lattice strain and distortions that interfere with the oriented attachment or aggregation of nanoparticles. As a result, the final particles exhibit more uniform size distribution and reduced agglomeration. This behaviour has also been reported in other doped cathode materials [40–42], where transition metal dopants act as grain growth inhibitors by modifying diffusion pathways during synthesis.

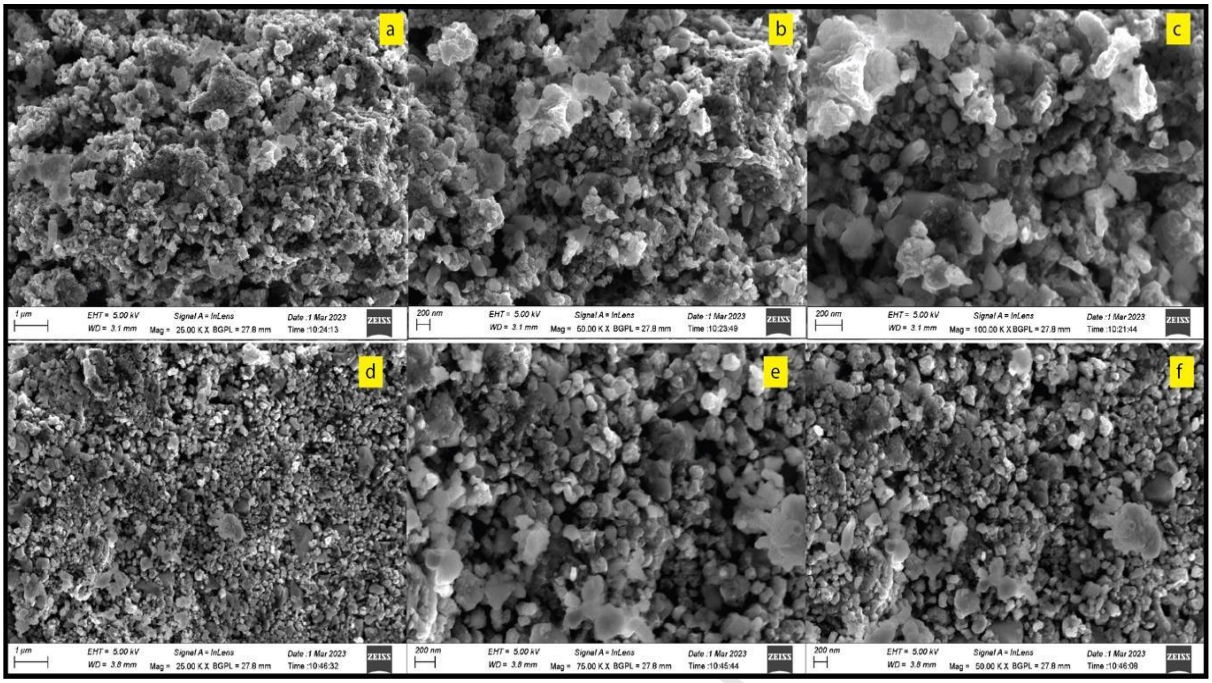

Fig. 2 FESEM images of $LiFePO_4$/C (a-c) and Ni-doped $LiFePO_4$/C (d-f)

Further, High Resolution TEM images of both the samples were presented in Fig. 3. Moreover, LFP/C reveals a primary particle size of 50 to 100 nm (Fig. 3(a1)), with a carbon coating of ~5 nm thickness ((Fig. 3(b1)). Distinct lattice fringes shown in Fig. 3(c1) with d spacing value of 2.17 Å corresponding to (311) plane. SAED pattern shown in Fig. 3(d1-e1) confirms the polycrystalline formation. Corresponding mapping results shown in Fig. 3(f1-j1), and EDS maps (Fig. 3(k1)) confirms the presence of all the elements in the LFP/C. Core-shell structured Ni-LFP/C shown in Fig. 3(a2) depicts the uniform carbon coating around core Ni-LFP/C. Carbon coating on the particles can be observed which is having thickness of ~4-5 nm (Fig. 3(b2)). As shown in Fig. 3(c2), lattice fringes with 1.305 Å represents (211) crystal plane. Polycrystalline Ni-LFP/C formation was witnessed with SAED pattern shown in Fig. 3 (d2-e2) with presence of ordered bright spots. The EDS map (Fig. 3(f2-k2)) shows a homogeneous distribution of dopants within the Ni-LFP/C sample. The presence of thin layer homogeneous carbon coating and Ni^{2+} -ions doping in Fe^{2+} sites of LFP synergistically contributing for the increase in ionic and electronic conductivity and thereby exhibit promising electrochemical performance. The HRTEM images of Ni-LFP/C measured at different parts of the material presented in Fig.S1. The figure clearly unveils the homogeneous spreading of carbon coating and the presence of a thin layer (5 nm) of carbon all around LFP particles. The carbon coating on LFP particles can be seen as core-shell structure, core being LFP material and thin carbon layer presumed as shell on core LFP material. Despite increasing the electronic conductivity, carbon coating on LFP particles mitigate the LFP grain growth during heating, and avoid direct

contact of electrodes with electrolyte. Furthermore, to assess the impact of thickness of carbon coating and its distribution, Ni-LFP/C material has been synthesized by varying the concentration (10 wt%, 15 wt%, and 20 wt%) of carbon precursor and the resulting materials were characterized by HR-TEM and C-S sulphur analysis to identify the variation in the thickness of carbon coatings and carbon content. Further, HR-TEM studies on doped LFP synthesized with different carbon concentration were shown in Fig.S2. When the lower concentration (i.e. 10 wt%) of carbon precursor used for the synthesis of Ni-LFP/C, non-uniform distribution of carbon layer on LFP particle was observed. The thickness of the carbon layer around the LFP particle is measured to be ~2 nm (Fig.S2(a1- a4)). Such kind of non-uniformity and lower carbon thickness causes poor electronic conduction and metal ion dissolution in electrolyte respectively. The HRTEM images of Ni-LFP/C with 15 wt% concentration of carbon precursor showed the presence of homogeneous carbon coating with a carbon layer of approximately 5 nm thickness on LFP particles (Fig. S2(b1-b4)).

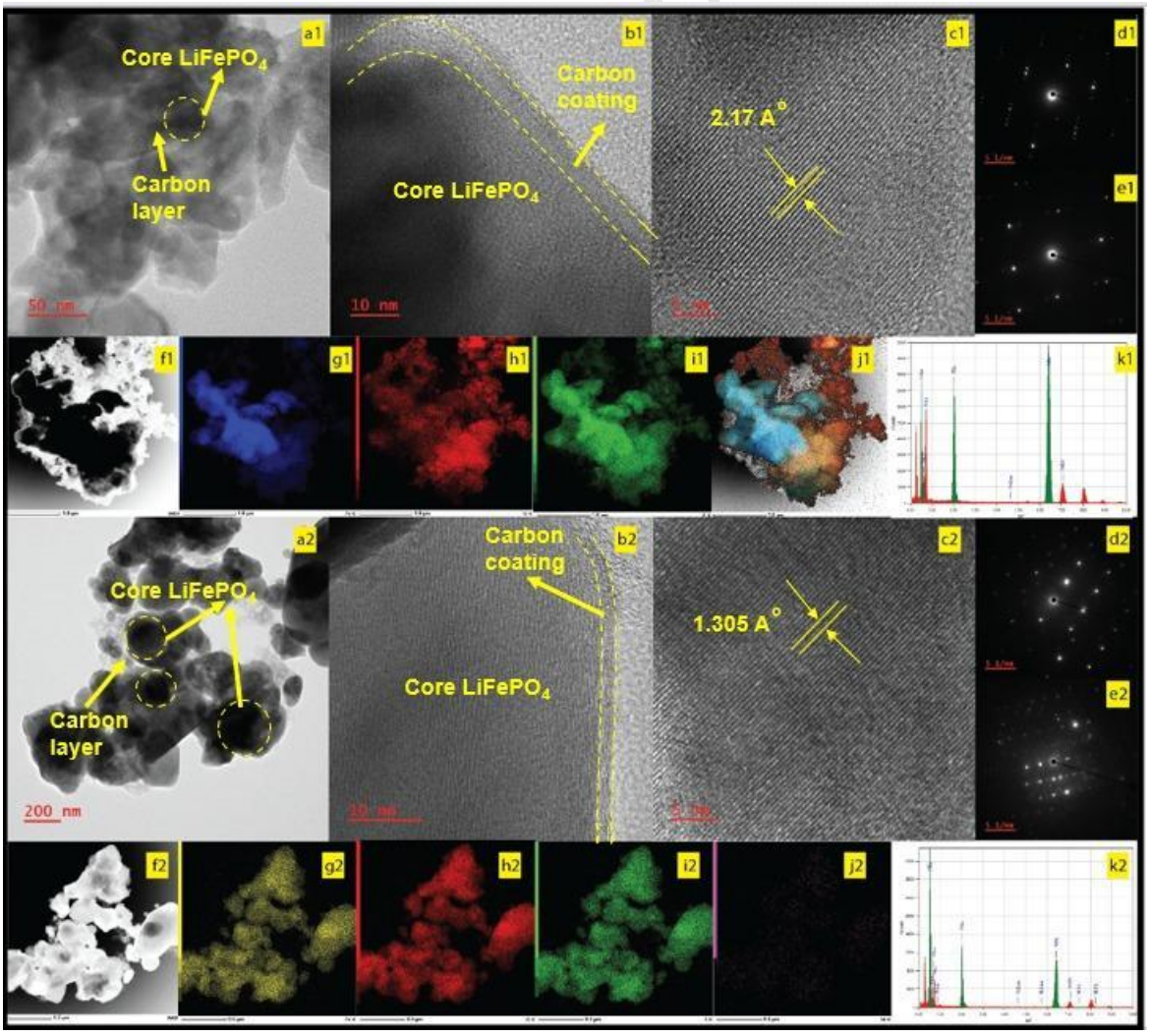

Fig. 3 HR-TEM analysis of $LiFePO_4$/C (a1-k1) and Ni-doped $LiFePO_4$/C (a2-k2)

When, further increasing the carbon content (i.e. 20 wt%), the formation of thicker carbon coating of ~ 10 nm observed on LFP particle as shown in Fig. S2(c1 and c4). In general, the thickness and distribution of carbon greatly influence the materials physico-chemical characteristics and its electrochemical performance as reported previously for carbon coated LFP [12]. Homogeneous carbon coating on the particles aids in improving the electronic conductivity by reducing the interparticle resistance for electron flow and thus improve the electrochemical performance. Further, ICP-OES analysis of Ni-LFP resulted in weight percent (wt%) of Fe, Li, Ni, and P elements as follows, i.e., 30.46, 4.16, 0.32, and 16.16 respectively. The carbon content measured by C-S analysis, for Ni-LFP/C with 10 wt%, 15 wt%, and 20 wt% carbon precursor is 2.8%, 3.7% and 4.3%. The high carbon content resulting in thicker carbon coating on LFP particles leads to slower Li-ion diffusion and thus low energy density, as it possesses a high amount of porous carbon. Hence, among all Ni-LFP/C materials, Ni-LFP/C material with 15 wt% carbon concentration possessing uniform carbon coating with optimized thickness is expected to result in enhanced performance. Accordingly, in view of the benefits and shortcomings of carbon, Ni-LFP/C with 15 wt% carbon concentration is considered as material of interest in the current study. The ICP-OES analysis shows Fe, Li, Ni and P in the amount of 30.46, 4.16, 0.73 and 16.16%, respectively. The amount while in LFP/C was estimated to be 4.2, 34.1 and 19.6% for Li, Fe and P, respectively. The ICP-OES analysis as well as the EDS mapping images shows the existence of Ni in very dilute concentration.

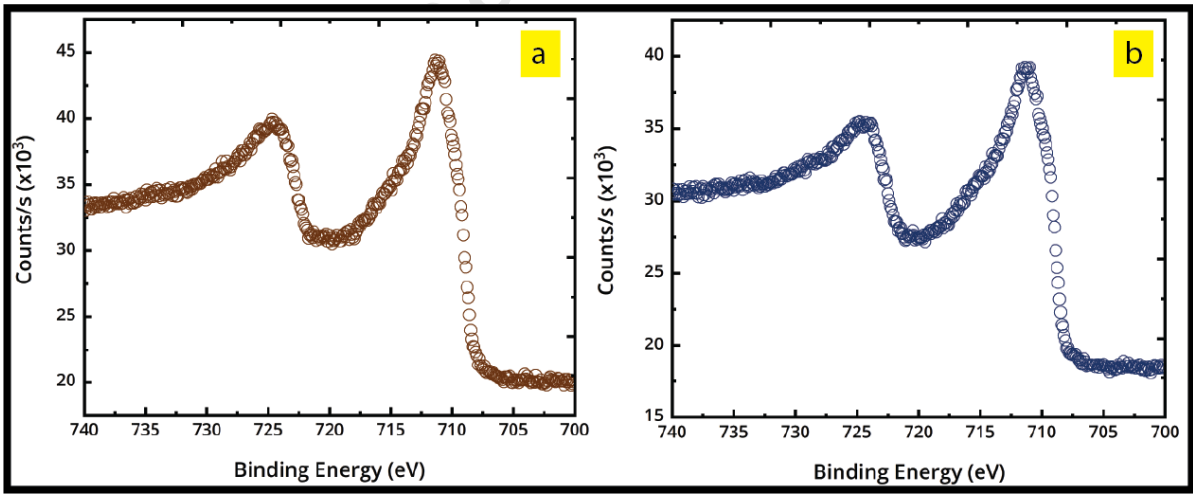

Fig. 4 XPS core-level Fe $2p$ scan of $LiFePO_4$/C (a) and Ni-doped $LiFePO_4$/C (b)

The XPS analysis is performed to identify the nature of elements and to determine the oxidation of both samples Fig. 4(a, b). For the sample LFP/C, concerned peaks for Fe $2p_{3/2}$ and Fe $2p_{1/2}$ are located at 711.39, and 724.45 eV sequentially. The deconvoluted core level Fe $2p$ spectra (Fig S4) with presence of Fe $2p_{3/2}$: ~709–711 eV, and Fe $2p_{1/2}$: ~722–725 eV with difference

in the binding energy of 13 eV clearly shows the presence of Fe in the Fe^{2+} oxidation state. Additionally, the XPS survey spectrum has been added to the Supporting Information (Fig S5) to confirm the elemental composition and to demonstrate the absence of any unexpected elements. Similarly, for Ni-LFP/C the peaks are followed at 711.22 and 724.28 eV for Fe $2p_{3/2}$ and Fe $2p_{1/2}$, respectively. This shows that Fe in both the synthesized samples (with and without doping) are present in divalent state [43]. Regarding the Ni^{2+} signal, we note that Ni was not clearly detected in the XPS spectra, likely due to its low doping concentration (1 mol%) and the surface-sensitive nature of XPS. Since Ni is present in a very small amount and primarily incorporated within the bulk crystal structure, its surface concentration may fall below the XPS detection limit. However, the presence of Ni in the material has been independently confirmed through ICP-OES analysis, which provides more accurate bulk elemental quantification. This clarification has also been included in the revised manuscript. Fig. 5(a, b)) shows the isotherms derived from N_2 adsorption-desorption experiments. Both the cathode materials show a type IV isotherm with H3 hysteresis loop [44]. The LFP/C cathode material shows a BET surface area of 61.6 m^2 g^{-1} with mean pore radius of 81.3 Å, while the Ni- LFP/C cathode material shows a SSA of 70.57 m^2 g^{-1} with an average pore radius of 68.9 Å. The increased specific surface area in Ni-doped $LiFePO_4$/C can be explained by two synergistic effects. First, nickel species act as a catalyst during calcination, promoting partial graphitization and modifying the carbonization pathway of the carbon precursor; catalytic graphitization produces thinner, more ordered carbon and alters surface morphology of the particles. Second, Ni incorporation into the LFP lattice induces local strain and modifies surface energies during crystallization, which suppresses grain growth and particle coalescence, yielding smaller primary particles and less agglomeration. Together these effects produce a higher surface area and a carbon coating with improved electronic connectivity, both of which contribute to the observed enhanced rate performance [45,46]. In addition, the pore volume (DFT method) of LFP/C and Ni-LFP/C is 0.205 and 0.213 cc g^{-1}, respectively.

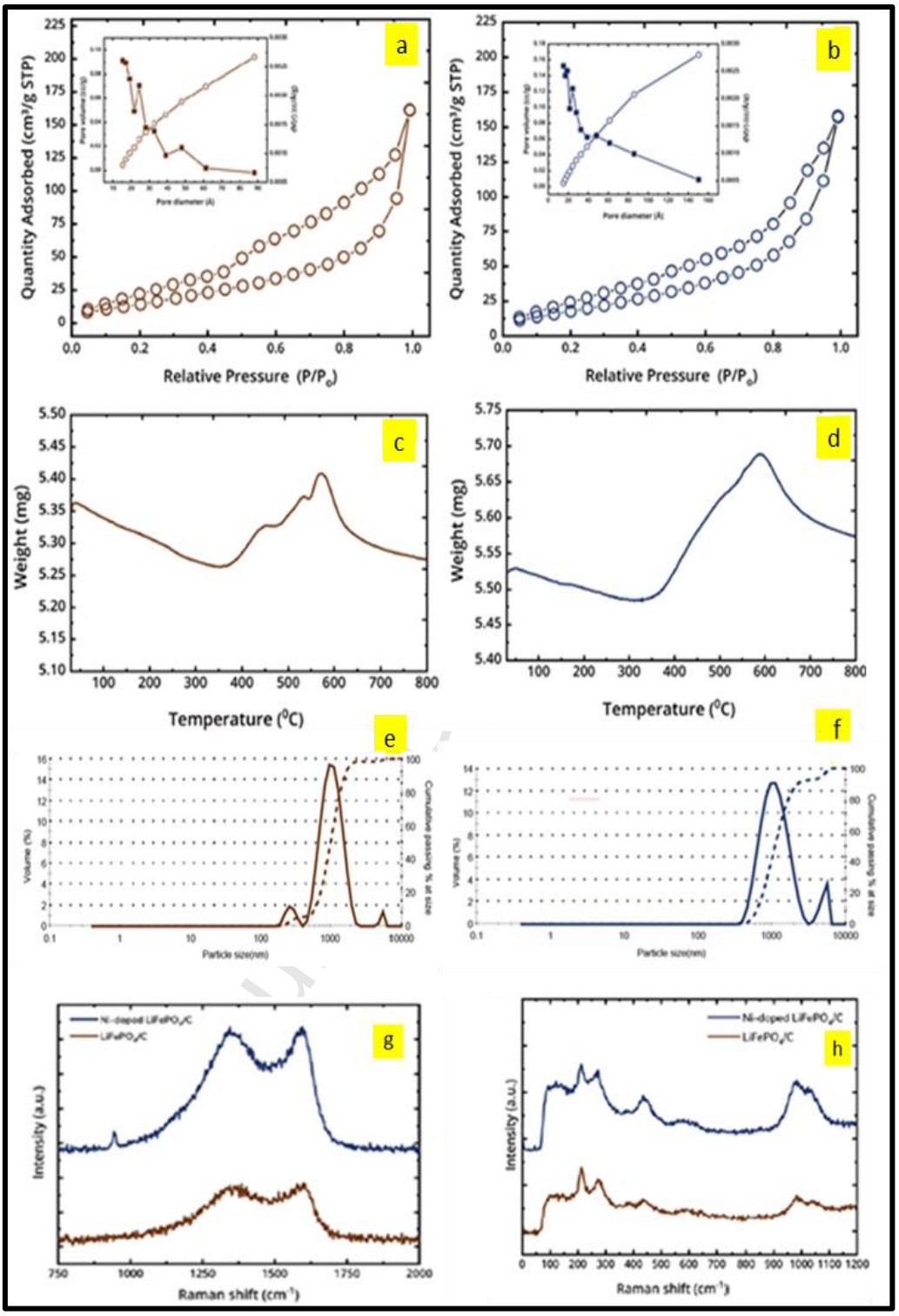

Fig. 5 BET isotherms (a-LFP/C, b-Ni-LFP/C), TGA (c-LFP/C, d-Ni-LFP/C), particle size distribution (e-LFP/C, f-Ni-LFP/C) and Raman spectra (g, h) of the prepared samples

The mesopores likely resulted from the expulsion of gas (CO_2) during the carbothermal reduction with citric acid, leaving behind a high number of small voids. The TGA thermogram

for both pristine and doped samples are displayed in Fig. 5 (c, d). We can observe some phase transition regions in both the thermograms. During the initial phase, from RT-300 ℃. The material undergoes dehydration and loses all water molecules. Thereafter, the material is oxidized to form $Li_3Fe_2(PO_4)_3$ and Fe_2O_3, which can be observed from the weight gain around 400-600 ℃. Lastly, the material experiences weight loss after complete combustion of carbon around 600-800 ℃ [47]. Corresponding particle size histograms (Fig. 5(e,f)) measured from DLS for LFP/C and Ni-LFP/C representing the μm (D_{50}) sized particles formation as discussed earlier. Raman spectroscopy was employed to gain insights into uniformity of carbon coating for both the samples. As depicted in Fig. 5(g,h), Raman spectra resulting in peaks in the wave number ranging from ~100-700 cm^{-1} indicates Fe-O vibrational peaks, whereas Raman shift at 900-1100 cm^{-1} is due to PO_4 vibrations respectively for $LiFePO_4$/C and Ni-doped $LiFePO_4$/C. Both samples exhibited D and G bands of carbon at following wavenumber i.e., at 1300, and 1600 cm^{-1} consecutively [48,49]. Additionally, the I_D/I_G ratio, which is considered as an indicator of degree of carbon graphitization measured to be 0.99 and 0.96 for LFP/C and Ni-LFP/C respectively. Following studies indicate that Ni-LFP/C exhibits a higher degree of graphitization, contributing to enhanced electronic conductivity and superior electrochemical performance [50,51]. The reason for higher degree of graphitization in the Ni doped material could be related to catalytic graphitization occurring during calcination, facilitated by the presence of Ni metal-ions, that used as a dopant source in the present study [52]. Though an amorphous layer of carbon forms during the initial calcination process, continuous calcination allows amorphous layers to dissolve into nickel catalyst and form as graphitic layer carbon. Further, these layers will be moved towards the particle surface and act as bridges for electron transfer. Nevertheless, the quantity and quality of coating carbon coating performs a significant role in the electrochemical properties of material. If the carbon coating is thin and non-homogenous, then the transport of electrons is affected in the uncoated region as it slows down Li^+ diffusion. The thin layer carbon coating also results in metal dissolution in electrolyte and will reduce the cycle life. If thicker carbon coating forms, then the diffusion of Lithium ion through it will be slow. In addition to doping and carbon coating, the particle size of materials presents a vital role in enhancing the performance of material. With an optimal particle size, Li-ion diffusion channel length is reduced. Thus, the particle dimensions are playing an active role in achieving high-rate performance [53] in LIB during the charge/discharge process.

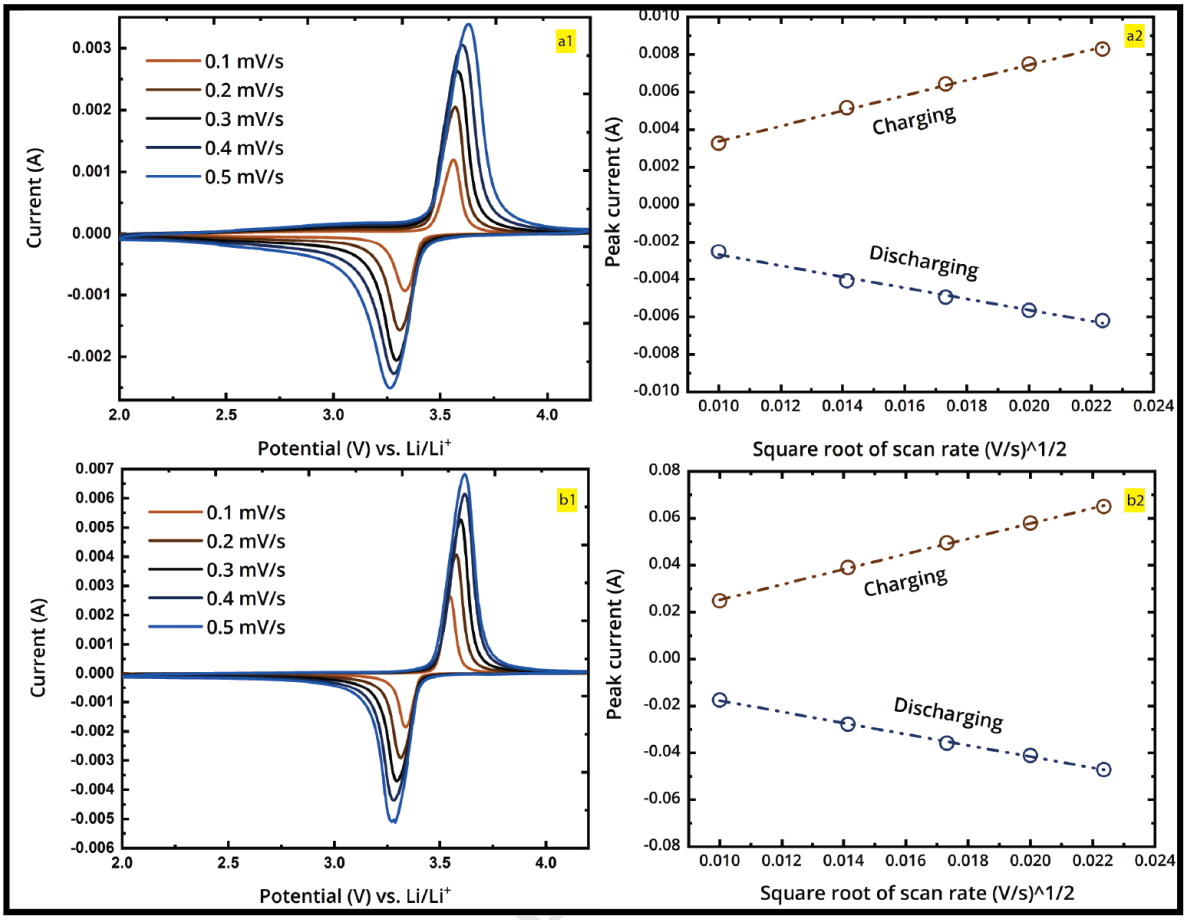

Fig. 6 Cyclic voltammetry scans of $LiFePO_4$/C (a1) and Ni-doped $LiFePO_4$/C (b1) electrodes measured at sweep rates; Linear curve plotted for peak current *vs.* square root of sweep rate for $LiFePO_4$/C (a2) and Ni-doped $LiFePO_4$/C (b2)

Cyclic voltammograms of pristine and doped LFP are displayed in Fig. 6 (a1, b1). Two samples with and without doping display the typical oxidation-reduction curves of $Fe^{2+/3+}$ occurring around 3.4 V. The Ni-LFP/C electrode exhibits an oxidation reaction peak of Fe ($Fe^{2+/3+}$) at 3.5 V, while reduction reaction peak ($Fe^{3+/2+}$) at 3.4 V. For the LFP/C electrode, oxidation and reduction peaks of Fe were observed at 3.6 V and 3.4 V (for 0.1 mV s^{-1} scan rate) [20,54]. The doping of Ni^{2+} has resulted in weaker polarization and enhanced reversibility of the Li-ions. This is also expected to increase the Li^+ diffusion kinetics. Cyclic voltammetry showing no peaks regarding Ni^{2+} implies that the dopant is not entirely participating in the redox reactions [53]. Furthermore, diffusion coefficient (D_{Li}) measured for Li^+ in LFP/C and Ni-LFP/C samples are estimated from the CV curves using Randles-Sevcik equation:

$$I_p = 2.687 \times 10^5 n^3 D^{1/2} A C \gamma^{1/2} \qquad \text{(Eq. 4.1)}$$

As shown in Eq. 4.1, I_p represents the peak current (A), n denotes the no. of electrons transferred (n=1) for $LiFePO_4 \leftrightarrow FePO_4 + e^- + Li^+$), A represents the area of the electrode (cm^2), C denotes Li-ion density (mol cm^{-3}) and γ represents the scan rate (V s^{-1}). Fig. 6 (a2, b2) show linear change in the current (I_p) *vs* square root of sweep rate ($\gamma^{1/2}$) for LFP/C and Ni-LFP/C electrodes. This implies the strong structural stability of active material during continuous lithiation and de-lithiation [55,56]. The D_{Li} for LFP/C and Ni-LFP/C samples are 9.1×10^{-11}, and 5.6×10^{-9} cm^2 s^{-1} correspondingly. Notably, the Ni-LFP/C sample exhibits two orders of higher Li^+ diffusion kinetics, indicating superior stability and reversibility. The increase in lithium-ion diffusion coefficient can be attributed to widening of the diffusion channel along [010] direction, with increase in Li-O bond lengths, and decrease in the bond lengths of P-O and Fe-O.

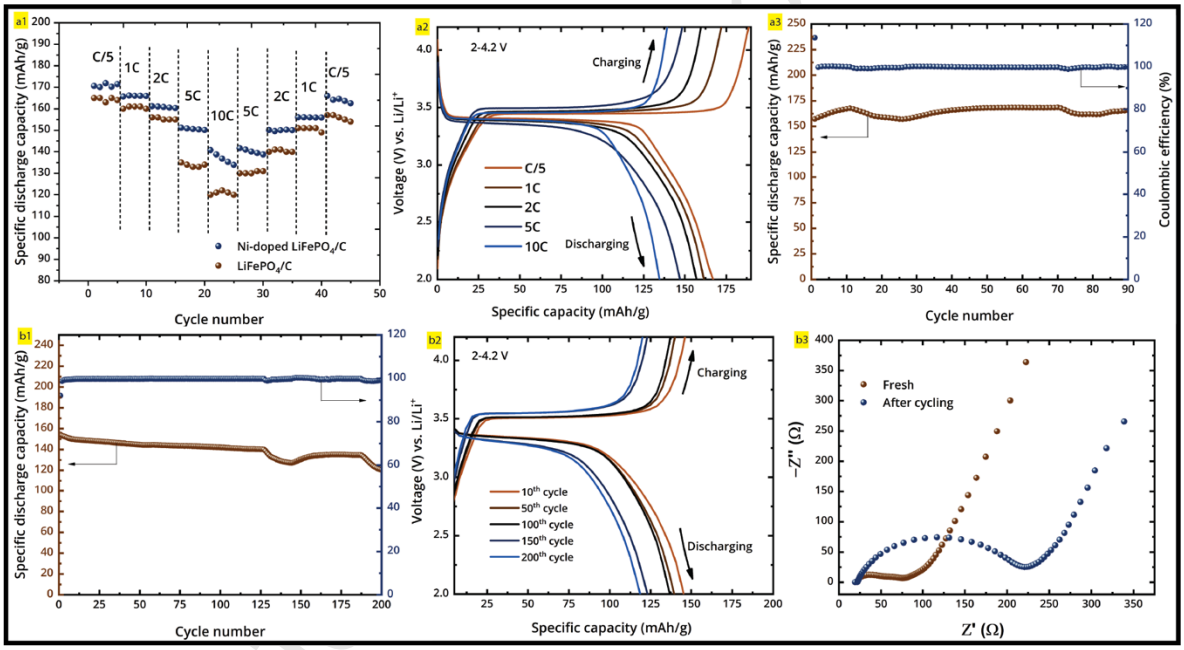

Fig. 7 Rate capability of $LiFePO_4$/C and Ni-LFP/C electrode (a1), Charge-Discharge studies (a2), Cyclic stability of Ni-LFP/C electrodes at 1C (a3), and 5C (b1); Charge-Discharge studies at 5C (b2) EIS analysis of fresh and cycled Ni-doped $LiFePO_4$/C electrodes (b3)

The charge and discharge profiles of LFP/C reveal that it delivers specific discharge capacities of 163, 160, 155, 133, and 120 mAh g^{-1} at C/5, 1C, 2C, 5C, and 10C, sequentially (Fig. 7(a1)). On the other hand, the Ni-LFP/C (15 wt%) electrode shows discharge specific capacities of 171, 166, 161, 150, and 136 mAh g^{-1} at the same C rates (Fig. 7(a2).

The theoretical capacity of $LiFePO_4$ is approximately 170 mAh g^{-1}, corresponding to the full extraction of one Li^+ ion per formula unit. In our study, the Ni-doped $LiFePO_4$/C sample delivered a slightly higher specific capacity of 171 mAh g^{-1} at C/5.

This marginal increase can be attributed to the synergistic effects of Ni doping, uniform carbon coating, and the incorporation of MWCNTs, which together enhance the electronic conductivity and improve the utilization of the active material. Ni doping may facilitate more efficient lithium-ion transport and reduce polarization, allowing the electrode to access near-complete lithium extraction more effectively. Additionally, surface capacitive contributions from the carbon matrix and MWCNTs may provide a minor boost to the overall capacity, especially at lower current rates. Further, half-cell results of Ni-LFP/C materials with different concentration of carbon precursors are shown Fig.S3. Ni-LFP/C with lower carbon content (10 wt%) delivers discharge capacities of 142,137,127,119, and 107 mAh g^{-1} at 0.1C, 0.2C, 1C, 2C, and 5C accordingly. While with high carbon content (20 wt%) exhibits inferior performance, i.e. 117,127,117,111, and 100 mAh g^{-1} measured at similar C rates, compared to other two (10 and 15 wt%) Ni-LFP/C materials. The lower capacities of Ni-LFP/C (10 wt% and 20 wt%) could be attributed to non-homogeneous and thicker coating on LFP particles, which results in low electronic and ionic conductivity and thus results in poor electrochemical performance. Ni-LFP/C (15%) exhibiting good rate capability, excellent cyclic stability and high specific capacity, owing to homogeneous and thin layer carbon coating is found to be consistent with the literature reported previously [12]. Impressively, the Ni-LFP/C electrode demonstrates higher performance than the LFP/C electrode, including specific capacity and rate capability (136 mAh g^{-1} at 10C). This enhanced rate performance for Ni-LFP/C is supported from improved intrinsic electronic conduction from the uniform dopant distribution and the widened [010] Li^+ diffusion channel achieved through controlled doping. For assessing the cycling stability of Ni-LFP/C electrode, the cells underwent charging and discharging at C/10 for the first four cycles, followed by 1C cycling for 90 cycles (Fig. 7(a3)). The Ni-LFP/C electrode exhibits excellent cyclic stability without any capacity fading as shown in Fig. 7(b1). Ni-LFP/C electrode demonstrates appreciable cycling performance at 5C current rate with cycling as depicted in Fig. 7(b2). Notably, after 200 charge-discharge cycles, the Ni-LFP/C electrode retains a specific discharge capacity of ~ 120 mAh g^{-1} at 5C, representing more than 80% capacity retention. We have compared the electrochemical performance of Ni-LFP/C reported in the present study with metal ion doped LFP available in the state of art literature as shown in the Table S1. Among the doped LFP cathode materials listed in Table S1, Ni-doped LFP exhibited prominent rate performance than others. Further, it also shown exceptional rate

performance of 136 mAh g^{-1} at 10C (6 min for charging/discharging) with a stable potential curve at 3.3 V, owing to formation of pure LFP with smaller particle size of ~ 1 μm. Also, the presence of homogeneous and thin layer (~ 4 nm) carbon coating around LFP particles enhances the electronic conductivity of LFP and regulates the LFP grain growth during heating by maintaining the reducing atmosphere. Further, the uniform distribution of Ni^{2+} in LFP enhances the electronic and Li-ion conductivity of Ni-LFP/C owing to its high electronegativity over Fe and widening of Li-ion diffusion channels along {010} direction by reducing the bonds of lengths of Fe-O and P-O, increasing the bond length of Li-O in crystal structure of LFP upon Ni^{2+} ion doping into Fe^{2+} ions of LFP. Thus, the above-mentioned physico-chemical characteristics of Ni doped LFP evident for exhibiting superior electrochemical performance compared with other doped LFP materials demonstrated in the literature. The enhanced cycling performance of the Ni-LFP/C electrode is because of its phase purity, uniform dopant distribution, and increased electronic and ionic conductivity facilitated by the thin layer of carbon-coating and Ni^{2+} doping. The analysis on EIS data represented in Fig. 7(b3) can be viewed in the further discussions.

When Ni^{2+}-ions doped into Fe^{2+}-ions site of LFP, the average bond distances of the phosphorous-oxygen (P-O) reduced from 1.56 to 1.54 Å, and iron-oxygen (Fe-O) bond lengths reduced to 2.22 from 2.15 Å, whereas the average bond length of lithium-oxygen (Li-O) increased from 2.07 to 2.16 Å. The shortened P-O bond results in increased stability of the phosphate $(PO_4)^{3-}$ framework that improves the cyclic performance of LFP [22,57]. Also, the reduction of Fe-O and P-O bonds, and expansion of Li-O bonds pave the way for widening of Li^+ diffusion channel along [010] direction results in fast diffusion of Li^+ [58].

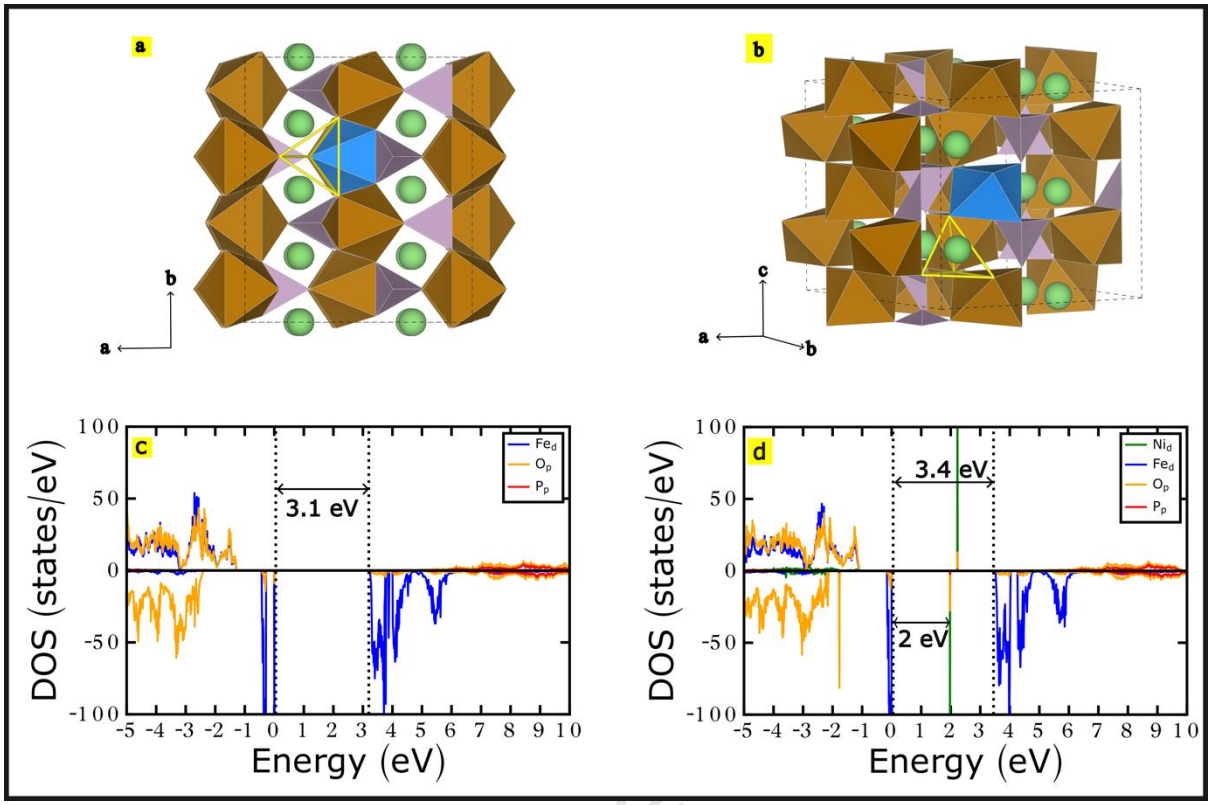

Fig. 8 Unit cell of the Ni-doped LFP marked by dashed lines with (a) c-axis going into the figure and (b) perspective view where Li ions are green spheres, Fe-O octahedra (Fe in the centre and O at the vertices) are brown, Ni-O octahedra (Ni in the centre and O at the vertices) are blue and the tetrahedral void through which Li migrates has yellow edges. Density of states (DOS) of (c) LFP (d) Ni-doped LFP.

Our DFT calculations reveal a contraction in the Ni-O octahedron compared to the Fe-O octahedra (~5.3% decrease in the NiO_6 octehadral volume compared to FeO_6) in Ni-LFP, in qualitative agreement with our Rietveld refinement (Table 1). This contraction causes a slight change in the (about 0.01 Å) bond distances between some Fe-O, Li-O, and P-O bonds for octahedra and tetrahedra that surround the Ni, although these changes are too small to explain the enhancement of Li diffusion. However, Ni-doping facilitates an expansion of ~1.4% in the volume of the intermediate tetrahedral site (4.22 $Å^3$ in Ni-LFP versus 4.16 $Å^3$ in LFP), that crucially influences the migration barrier that Li-ions have to overcome while diffusing within the LFP structure [59]. This tetrahedral site is illustrated by yellow edges in panels a and b of Fig. 8. Given that an expansion of the intermediate site during Li^+ migration should reduce electrostatic repulsion from nearby transition metal and P^{5+} cations [60], we expect Ni-addition to cause an associated decrease in the Li-migration barrier, resulting in an improvement in Li-diffusivity and power performance that is consistent with our experimental observation. Another factor that can contribute to electrode performance with doping is changes to

electronic structure and/or conductivity. Thus, we calculated the electronic DOS in both pristine LFP and Ni-doped LFP, which are plotted in panels c and d of Fig. 8, correspondingly. Blue, orange, red, and green curves indicate Fe *d*, O *p*, P *p*, and Ni *d* states, respectively, while the vertical dotted lines signify valence and conduction band edges. The zero on the energy scale is arbitrarily set to the valence band maximum. Importantly, our DOS calculations predict a band gap of 3.1 eV in pristine-LFP, which underestimates the experimental gap of ~3.8 eV [61], but is expected given that DFT is a ground-state theory known to underestimate band gaps. Importantly, Ni-addition introduces states within the gap that are ~2 eV from the valence band edge and ~1 eV from the conduction band edge. Thus, Ni-doping promotes the availability of free electrons in the structure and acts as a *n*-type dopant. As a result, Ni-doping enhances the electronic conductivity for LFP, which may contribute to both better cycle life and power performance.

Further, the high electronegativity of Ni compared to Fe (Electro-negativity order: Mn<Fe<Co<Ni) [62] helps Ni^{2+} to behave like a strong pillar in the crystal structure. Ni^{2+} possessing high electron affinity helps to form a strong bond with electrons and stabilize the LFP structure without any deformation during the charging and discharging process. Thus, the low atomic radii (i.e. 0.69 Å) of Ni^{2+} compared to higher atomic radii (0.74 Å) of Fe^{2+} and high electronegativity of Ni^{2+} ions LFP results in the reduction in the unit cell dimensions and improved electronic conductivity, which attributed to the enhanced electrochemical performance of Ni-LFP/C. EIS analysis was carried out to investigate the charge-transfer resistance of the Ni-doped $LiFePO_4$/C electrode before and after long cycle performance (5C for 200 cycles). EIS data of the Ni-LFP/C electrode (Fig. 7(b3)) exhibit a half-circle in the medium frequency, and an inclined line (at 45º) in the low-frequency range. The EIS data shows that the charge-transfer resistance increased from 73 to 222 Ω after long-term cycling at high current rate. This might be because of certain side reactions with Ni-LFP/C and the electrolyte, which results in higher impedance inside the cell.

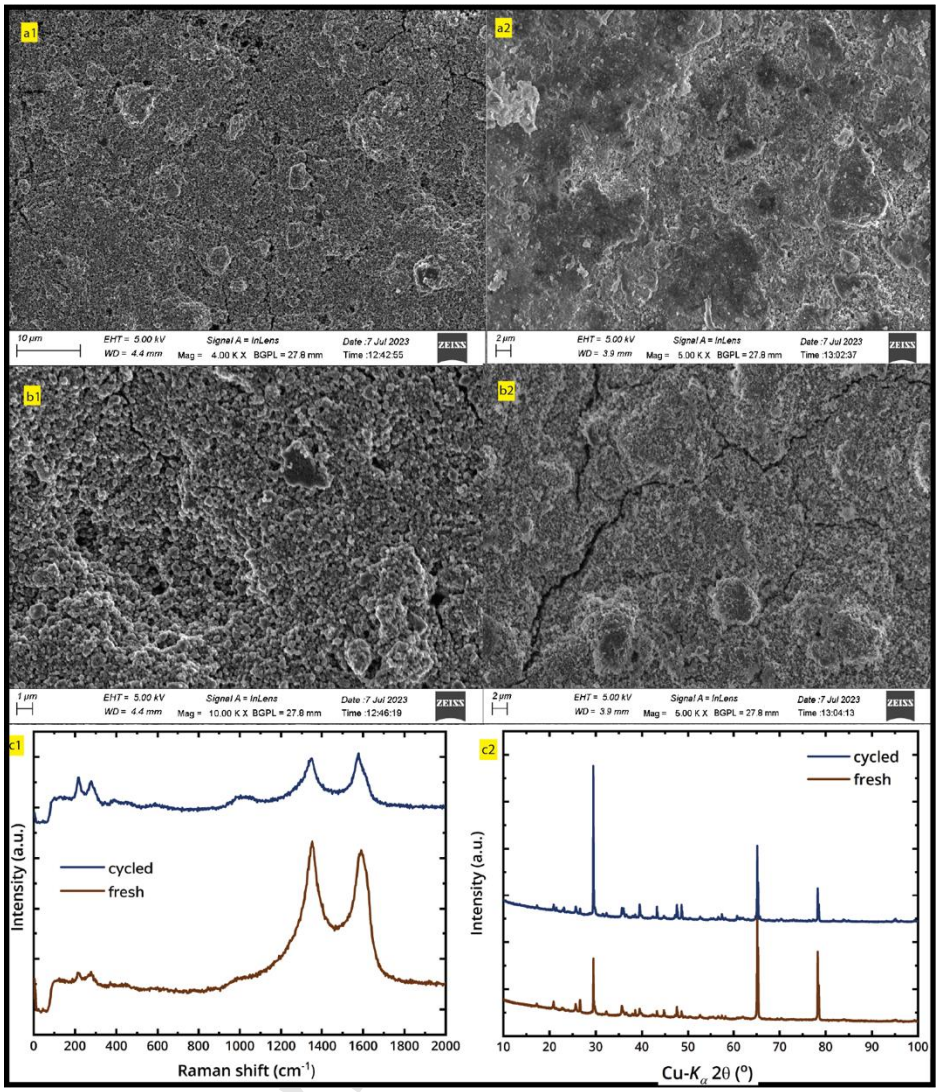

Fig. 9 FESEM images (a1,a2 and b1, b2), Raman spectra (c1) and XRD patterns (c2) of Ni-LFP/C electrode after 200 cycles at 5C.

The overall post-mortem analysis shows that the Ni-LFP/C electrode is quite stable even after fast charging for several hundreds of cycles. From the FE-SEM it is observed that, compared to pristine electrodes (Fig. 9(a1-a2), PC-washed cycled electrodes (Fig. 9 (b1-b2)) display very minor structural transformations. The FESEM images of the cycled electrode also show small cracks and separator material intact with the active material. The cracks shown here might have occurred due to long-term cycling or while disassembling/washing the electrode. The microcracks observed in the FESEM image of the PC-washed, cycled electrodes in Fig. 9(b2) are primarily the result of repeated volume changes during high-rate cycling. These cracks are generally considered detrimental to long-term performance, as they can disrupt the structural integrity of the electrode, degrade electrical contact between active material and the conductive network, and hinder efficient Li^+ diffusion. Over extended cycling, this can contribute to capacity fading and reduced Coulombic efficiency. The Raman (Fig. 9(c1)) and XRD (Fig.

9(c2)) spectra show no change or addition in the peaks, depicting no structural transformations or significant chemical reactions. Further, benchmarking studies were carried out using commercial LFP as shown in Fig S6. Electrochemical tests show that (Fig S6) the Ni-doped LFP synthesized in this work delivers a specific capacity of 168 mAh g^{-1} at 1C, whereas commercial LFP exhibits a lower capacity of 132 mAh g^{-1} at 1C. This enhanced capacity reflects a significant improvement in energy density, which is crucial for developing high-capacity lithium-ion cells. In addition to improved energy density, the Ni-doped LFP also demonstrates superior rate performance. At a high current rate of 10C, it maintains a specific capacity of 136 mAh g^{-1}, indicating excellent high-rate capability and fast charge-discharge performance. These results suggest that Ni-doping not only boosts the intrinsic energy storage capability of LFP but also enables rapid power delivery and reduced charging time, which are highly desirable for modern high-performance lithium-ion batteries.

4. Conclusions

In the present study, we successfully synthesized carbon-coated Ni^{2+}-doped $LiFePO_4$ (Ni-LFP/C) using a simple, cost-effective, and scalable solid-state ball milling process, achieving a pure olivine-type LFP phase. Morphological analysis revealed a pulverized structure characteristic of the ball milling route, with particle sizes estimated to be around 1 μm. High-resolution TEM-EDX mapping confirmed uniform dopant distribution, while XPS analysis indicated that iron remained in the divalent oxidation state. Cyclic voltammetry results showed reduced electrode polarization and lower charge transfer resistance due to Ni^{2+} doping. Galvanostatic charge–discharge (GCD) tests demonstrated high discharge capacities of 171, 166, 161, 150, and 136 mAh g^{-1} at C/5, 1C, 2C, 5C, and 10C, consecutively. Notably, at a high current rate of 5C, Ni-LFP/C retained over 80% of its capacity after 200 cycles. In conclusion, Ni^{2+}-doped $LiFePO_4$/C exhibited markedly enhanced electrochemical performance, including excellent rate capability, high specific capacity, and exceptional cycle stability. This improved performance is owed to the substitution doping of Fe^{2+} by Ni^{2+}, which led to a reduced unit cell volume, shortened P–O and Fe–O bonds, and elongated Li–O bonds. These structural changes expanded the Li^+ diffusion channels in the [010] direction, resulting in a two-order magnitude increase in lithium-ion diffusion kinetics (5.6×10^{-9} cm^2 s^{-1}) compared with pure LFP (9.1×10^{-11} cm^2 s^{-1}). The exceptional rate performance could be ascribed to the combined effects of Ni^{2+} doping, smaller particle size, homogeneous thin carbon coating, and reduced charge transfer resistance. Overall, this study presents a synergistic approach to synthesize high-performance Ni-LFP/C cathodes, well-suited for the fabrication of high-rate lithium-ion batteries used in

electric vehicles, portable electronics, and grid energy storage applications. Moreover, the synergistic approach demonstrated here can be extended to other cathode and anode materials for the development of next-generation high-power LIBs.

References

[1] L.-X. Yuan, Z.-H. Wang, W.-X. Zhang, X.-L. Hu, J.-T. Chen, Y.-H. Huang, J.B. Goodenough, Development and challenges of $LiFePO_4$ cathode material for lithium-ion batteries, Energy Environ. Sci. 4 (2011) 269–284. https://doi.org/10.1039/C0EE00029A.

[2] K. Dokko, S. Koizumi, K. Sharaishi, K. Kanamura, Electrochemical properties of LiFePO4 prepared via hydrothermal route, J Power Sources 165 (2007) 656–659. https://doi.org/10.1016/j.jpowsour.2006.10.027.

[3] J. Zheng, X. Li, Z. Wang, H. Guo, S. Zhou, LiFePO4 with enhanced performance synthesized by a novel synthetic route, J Power Sources 184 (2008) 574–577. https://doi.org/10.1016/j.jpowsour.2008.01.016.

[4] J. Li, Z.-F. Ma, Past and Present of $LiFePO_4$: From Fundamental Research to Industrial Applications, Chem 5 (2019) 3–6. https://doi.org/10.1016/j.chempr.2018.12.012.

[5] W.-J. Zhang, Structure and performance of LiFePO4 cathode materials: A review, J Power Sources 196 (2011) 2962–2970. https://doi.org/10.1016/j.jpowsour.2010.11.113.

[6] D. Jugović, D. Uskoković, A review of recent developments in the synthesis procedures of lithium iron phosphate powders, J Power Sources 190 (2009) 538–544. https://doi.org/10.1016/j.jpowsour.2009.01.074.

[7] G.X. Wang, S. Needham, J. Yao, J.Z. Wang, R.S. Liu, H.K. Liu, A study on $LiFePO_4$ and its doped derivatives as cathode materials for lithium-ion batteries, J Power Sources 159 (2006) 282–286. https://doi.org/10.1016/j.jpowsour.2006.04.046.

[8] K. Zaghib, M. Simoneau, M. Armand, M. Gauthier, Electrochemical study of $Li_4Ti_5O_{12}$ as negative electrode for Li-ion polymer rechargeable batteries, J Power Sources 81–82 (1999) 300–305. https://doi.org/10.1016/S0378-7753(99)00209-8.

[9] A. Yamada, S.C. Chung, K. Hinokuma, Optimized $LiFePO_4$ for lithium battery cathodes, J Electrochem Soc 148 (2001) A224–A229. https://doi.org/10.1149/1.1348257.

[10] R. Dominko, M. Bele, M. Gaberscek, M. Remskar, D. Hanzel, S. Pejovnik, J. Jamnik, Impact of the Carbon Coating Thickness on the Electrochemical Performance of $LiFePO_4$/C Composites, J Electrochem Soc 152 (2005) A607. https://doi.org/10.1149/1.1860492.

[11] M.M. Doeff, J.D. Wilcox, R. Kostecki, G. Lau, Optimization of carbon coatings on LiFePO4, J Power Sources 163 (2006) 180–184. https://doi.org/10.1016/j.jpowsour.2005.11.075.

[12] P.M. Pratheeksha, E.H. Mohan, B.V. Sarada, M. Ramakrishna, K. Hembram, P.V.V. Srinivas, P.J. Daniel, T.N. Rao, S. Anandan, Development of a novel carbon-coating strategy for producing core–shell structured carbon coated $LiFePO_4$ for an improved Li-ion battery performance, Physical Chemistry Chemical Physics 19 (2017) 175–188. https://doi.org/10.1039/C6CP06923A.

[13] X. Wu, Y. Guo, J. Su, J. Xiong, Y. Zhang, L. Wan, Carbon-Nanotube-Decorated Nano-$LiFePO_4$@C Cathode Material with Superior High-Rate and Low-Temperature Performances for Lithium-Ion Batteries, Adv Energy Mater 3 (2013) 1155–1160. https://doi.org/10.1002/aenm.201300159.

[14] L. Wang, W. Sun, X. Tang, X. Huang, X. He, J. Li, Q. Zhang, J. Gao, G. Tian, S. Fan, Nano particle $LiFePO_4$ prepared by solvothermal process, J Power Sources 244 (2013) 94–100. https://doi.org/10.1016/j.jpowsour.2013.03.101.
[15] H. Zhang, Z. Zou, S. Zhang, J. Liu, S. Zhong, A review of the Doping Modification of $LiFePO_4$ as a Cathode Material for Lithium Ion Batteries, Int J Electrochem Sci 15 (2020) 12041–12067. https://doi.org/10.20964/2020.12.71.
[16] C. Yan, K. Wu, P. Jing, H. Luo, Y. Zhang, Mg-doped porous spherical $LiFePO_4$/C with high tap-density and enhanced electrochemical performance, Mater Chem Phys 280 (2022) 125711. https://doi.org/10.1016/j.matchemphys.2022.125711.
[17] N. Shaji, F. Jiang, J.Y. Sung, M. Nanthagopal, T. Kim, B.J. Jeong, S.P. Jung, C.W. Lee, Heteroatoms-doped carbon effect on $LiFePO_4$ cathode for Li-ion batteries, J Energy Storage 72 (2023) 108710. https://doi.org/10.1016/j.est.2023.108710.
[18] S. Karimzadeh, B. Safaei, W. Huang, T.-C. Jen, Theoretical investigation on niobium doped $LiFePO_4$ cathode material for high performance lithium-ion batteries, J Energy Storage 67 (2023) 107572. https://doi.org/10.1016/j.est.2023.107572.
[19] B. Ramasubramanian, S. Sundarrajan, V. Chellappan, M. V. Reddy, S. Ramakrishna, K. Zaghib, Recent Development in Carbon-LiFePO4 Cathodes for Lithium-Ion Batteries: A Mini Review, Batteries 8 (2022) 133. https://doi.org/10.3390/batteries8100133.
[20] Z. Xu, L. Gao, Y. Liu, L. Li, Review—Recent Developments in the Doped $LiFePO_4$ Cathode Materials for Power Lithium Ion Batteries, J Electrochem Soc 163 (2016) A2600–A2610. https://doi.org/10.1149/2.0411613jes.
[21] S.-P. Chen, D. Lv, J. Chen, Y.-H. Zhang, F.-N. Shi, Review on Defects and Modification Methods of $LiFePO_4$ Cathode Material for Lithium-Ion Batteries, Energy and Fuels 36 (2022) 1232–1251. https://doi.org/10.1021/acs.energyfuels.1c03757.
[22] X. Liu, Y. Zhang, Y. Meng, T. Kang, H. Gao, L. Huang, F. Zhu, Influence Mechanism of Mg 2+ Doping on Electrochemical Properties of $LiFePO_4$ Cathode Materials, ACS Appl Energy Mater 5 (2022) 8452–8459. https://doi.org/10.1021/acsaem.2c00986.
[23] T. Teng, L. Xiao, L. Shen, G. Qiu, J. Ran, X. Guo, Y. Zhu, H. Chen, Effect of Nb doping at Fe site on the cycling stability and rate capability of $LiFePO_4$ for lithium-ion batteries, Vacuum 203 (2022) 111306. https://doi.org/10.1016/j.vacuum.2022.111306.
[24] S. Jiang, Y. Wang, Synthesis and characterization of vanadium-doped $LiFePO_4$@C electrode with excellent rate capability for lithium-ion batteries, Solid State Ion 335 (2019) 97–102. https://doi.org/10.1016/j.ssi.2019.03.002.
[25] P. Hohenberg, W. Kohn, Inhomogeneous Electron Gas, Physical Review 136 (1964) B864–B871. https://doi.org/10.1103/PhysRev.136.B864.
[26] G. Kresse, J. Hafner, *Ab initio* molecular dynamics for liquid metals, Phys Rev B 47 (1993) 558–561. https://doi.org/10.1103/PhysRevB.47.558.
[27] G. Kresse, J. Furthmüller, Efficient iterative schemes for *ab initio* total-energy calculations using a plane-wave basis set, Phys Rev B 54 (1996) 11169–11186. https://doi.org/10.1103/PhysRevB.54.11169.
[28] G. Kresse, J. Hafner, *Ab initio* molecular dynamics for open-shell transition metals, Phys Rev B 48 (1993) 13115–13118. https://doi.org/10.1103/PhysRevB.48.13115.
[29] G. Kresse, D. Joubert, From ultrasoft pseudopotentials to the projector augmented-wave method, Phys Rev B 59 (1999) 1758–1775. https://doi.org/10.1103/PhysRevB.59.1758.
[30] V.I. Anisimov, J. Zaanen, O.K. Andersen, Band theory and Mott insulators: Hubbard *U* instead of Stoner *I*, Phys Rev B 44 (1991) 943–954. https://doi.org/10.1103/PhysRevB.44.943.

[31] S.L. Dudarev, G.A. Botton, S.Y. Savrasov, C.J. Humphreys, A.P. Sutton, Electron-energy-loss spectra and the structural stability of nickel oxide: An LSDA+U study, Phys Rev B 57 (1998) 1505–1509. https://doi.org/10.1103/PhysRevB.57.1505.
[32] J. Sun, A. Ruzsinszky, J.P. Perdew, Strongly Constrained and Appropriately Normed Semilocal Density Functional, Phys Rev Lett 115 (2015) 036402. https://doi.org/10.1103/PhysRevLett.115.036402.
[33] M. Hellenbrandt, The Inorganic Crystal Structure Database (ICSD)—Present and Future, Crystallogr Rev 10 (2004) 17–22. https://doi.org/10.1080/08893110410001664882.
[34] O.Y. Long, G. Sai Gautam, E.A. Carter, Evaluating optimal <math> <mi>U</mi> </math> for <math> <mrow> <mn>3</mn> <mi>d</mi> </mrow> </math> transition-metal oxides within the SCAN+ <math> <mi>U</mi> </math> framework, Phys Rev Mater 4 (2020) 045401. https://doi.org/10.1103/PhysRevMaterials.4.045401.
[35] G. Sai Gautam, E.A. Carter, Evaluating transition metal oxides within DFT-SCAN and <math> <mrow> <mtext>SCAN</mtext> <mo>+</mo> <mi>U</mi> </mrow> </math> frameworks for solar thermochemical applications, Phys Rev Mater 2 (2018) 095401. https://doi.org/10.1103/PhysRevMaterials.2.095401.
[36] C. Shen, G. Li, L. Liu, P. Li, H. Xu, H. Hu, L. Wang, Facile fabrication of compact $LiFePO_4$/C composite with excellent atomically-efficient for high-energy-density Li-ion batteries, J Power Sources 496 (2021) 229759. https://doi.org/10.1016/j.jpowsour.2021.229759.
[37] R.D. Shannon, Revised effective ionic radii and systematic studies of interatomic distances in halides and chalcogenides, Acta Crystallographica Section A 32 (1976) 751–767. https://doi.org/10.1107/S0567739476001551.
[38] B. Zhang, X. Ma, W. Hou, W. yuan, L. He, O. Yang, Y. Liu, J. Wang, Y. Xu, Revealing the Ultrahigh Rate Performance of the La and Ce Co-doping $LiFePO_4$ Composite, ACS Appl Energy Mater 5 (2022) 14712–14719. https://doi.org/10.1021/acsaem.2c02035.
[39] A. Hebert, E. McCalla, The role of metal substitutions in the development of Li batteries, part I: cathodes, Mater Adv 2 (2021) 3474–3518. https://doi.org/10.1039/D1MA00081K.
[40] L. Gao, Z. Xu, S. Zhang, The co-doping effects of Zr and Co on structure and electrochemical properties of LiFePO4 cathode materials, J Alloys Compd 739 (2018) 529–535. https://doi.org/10.1016/j.jallcom.2017.12.313.
[41] J. Tu, K. Wu, H. Tang, H. Zhou, S. Jiao, Mg–Ti co-doping behavior of porous $LiFePO_4$ microspheres for high-rate lithium-ion batteries, J Mater Chem A Mater 5 (2017) 17021–17028. https://doi.org/10.1039/C7TA04426G.
[42] K. Akhmetova, F. Sultanov, A. Mentbayeva, N. Umirov, Z. Bakenov, B. Tatykayev, Advances in multi-element doping of LiFePO4 cathode material for capacity enhancement in Li-ion batteries, J Power Sources 624 (2024) 235531. https://doi.org/10.1016/j.jpowsour.2024.235531.
[43] J. Ou, K. Li, H. Deng, B. Li, J. Cao, M. Li, Facilely synthesized $LiFePO_4$ nanocomposites with excellent electrochemical properties as cathodes for lithium ion batteries, New Journal of Chemistry 47 (2023) 3067–3074. https://doi.org/10.1039/D2NJ05537F.
[44] R. Bardestani, G.S. Patience, S. Kaliaguine, Experimental methods in chemical engineering: specific surface area and pore size distribution measurements—BET, BJH, and DFT, Canadian Journal of Chemical Engineering 97 (2019) 2781 – 2791. https://doi.org/10.1002/cjce.23632.

[45] F.J. Soler-Piña, J. Morales, Á. Caballero, Synergy between highly dispersed Ni nanocrystals and graphitized carbon derived from a single source as a strategy for high performance Lithium-Sulfur batteries, J Colloid Interface Sci 640 (2023) 990–1004. https://doi.org/10.1016/j.jcis.2023.03.035.

[46] A. Hebert, E. McCalla, The role of metal substitutions in the development of Li batteries, part I: cathodes, Mater Adv 2 (2021) 3474–3518. https://doi.org/10.1039/D1MA00081K.

[47] Q. Li, Z. Zhou, S. Liu, X. Zhang, Growth of FePO4 nanoparticles on graphene oxide sheets for synthesis of LiFePO4/graphene, Ionics (Kiel) 22 (2016) 1027–1034. https://doi.org/10.1007/s11581-016-1636-y.

[48] E. Markevich, R. Sharabi, O. Haik, V. Borgel, G. Salitra, D. Aurbach, G. Semrau, M.A. Schmidt, N. Schall, C. Stinner, Raman spectroscopy of carbon-coated $LiCoPO_4$ and $LiFePO_4$ olivines, J Power Sources 196 (2011) 6433–6439. https://doi.org/10.1016/j.jpowsour.2011.03.059.

[49] J. Wu, G.K.P. Dathar, C. Sun, M.G. Theivanayagam, D. Applestone, A.G. Dylla, A. Manthiram, G. Henkelman, J.B. Goodenough, K.J. Stevenson, *In situ* Raman spectroscopy of LiFePO 4 : size and morphology dependence during charge and self-discharge, Nanotechnology 24 (2013) 424009. https://doi.org/10.1088/0957-4484/24/42/424009.

[50] G. Chandra, S.J. Kashyap, S.S. Sreedhara, S. V. Bulusu, V.V. Ananthula, V. R., T.N. Rao, A. Srinivasan, Enhanced stability and high-yield $LiFePO_4$/C derived from low-cost iron precursors for high-energy Li-ion batteries, J Energy Storage 72 (2023) 108453. https://doi.org/10.1016/j.est.2023.108453.

[51] Y. Li, L. Wang, K. Zhang, F. Liang, Y. Yao, L. Kong, High performance of $LiFePO_4$ with nitrogen and phosphorus dual-doped carbon layer for lithium-ion batteries, J Alloys Compd 890 (2022) 161617. https://doi.org/10.1016/j.jallcom.2021.161617.

[52] Z. Yan, D. Huang, A. Lai, Y. Chu, F. Zheng, Y. Cai, Q. Pan, H. Wang, Y. Huang, Q. Li, Nickel catalyzed graphitized carbon coated $LiFe_{1-x}Ni_xPO_4$ composites as cathode material for high-performance lithium-ion batteries, Electrochim Acta 353 (2020) 136565. https://doi.org/10.1016/j.electacta.2020.136565.

[53] J. Ma, B. Li, H. Du, C. Xu, F. Kang, The Effect of Vanadium on Physicochemical and Electrochemical Performances of $LiFePO_4$ Cathode for Lithium Battery, J Electrochem Soc 158 (2011) A26. https://doi.org/10.1149/1.3514688.

[54] M.A.M.M. Alsamet, E. Burgaz, Synthesis and characterization of nano-sized $LiFePO_4$ by using consecutive combination of sol-gel and hydrothermal methods, Electrochim Acta 367 (2021) 137530. https://doi.org/10.1016/j.electacta.2020.137530.

[55] J. Geng, Z. Zou, T. Wang, S. Zhang, S. Zhong, W. Ling, X. Peng, X. Hu, Synthesis and electrochemical behavior of K+ and Mn2+ co-doped $LiFePO_4$/C as a cathode material for lithium-ion batteries and the mechanism of modification, Journal of Electroanalytical Chemistry 933 (2023) 117275. https://doi.org/10.1016/j.jelechem.2023.117275.

[56] M.A.M.M. AL-SAMET, E. Burgaz, Improving the lithium-ion diffusion and electrical conductivity of $LiFePO_4$ cathode material by doping magnesium and multi-walled carbon nanotubes, J Alloys Compd 947 (2023) 169680. https://doi.org/10.1016/j.jallcom.2023.169680.

[57] X. Liu, R. Zhao, Y. Xia, Q. Li, Improved electrochemical performance of $LiFePO_4$/carbon cathode for lithium-ion batteries, Ionics (Kiel) 28 (2022) 4579–4585. https://doi.org/10.1007/s11581-022-04715-z.

[58] J. Peng, Z. Li, Y. You, J. Liu, L. Wang, J. Xu, S. Ou, M. Yuan, Contribution of Ti-Doping to the Cyclic Stability of LiFe 0.6 Mn 0.4 PO 4 /C, Ind Eng Chem Res 63 (2024) 8228–8238. https://doi.org/10.1021/acs.iecr.4c00307.
[59] Z. Rong, R. Malik, P. Canepa, G. Sai Gautam, M. Liu, A. Jain, K. Persson, G. Ceder, Materials Design Rules for Multivalent Ion Mobility in Intercalation Structures, Chemistry of Materials 27 (2015) 6016–6021. https://doi.org/10.1021/acs.chemmater.5b02342.
[60] Z. Rong, R. Malik, P. Canepa, G. Sai Gautam, M. Liu, A. Jain, K. Persson, G. Ceder, Materials Design Rules for Multivalent Ion Mobility in Intercalation Structures, Chemistry of Materials 27 (2015) 6016–6021. https://doi.org/10.1021/acs.chemmater.5b02342.
[61] F. Zhou, K. Kang, T. Maxisch, G. Ceder, D. Morgan, The electronic structure and band gap of LiFePO4 and LiMnPO4, Solid State Commun 132 (2004) 181–186. https://doi.org/10.1016/j.ssc.2004.07.055.
[62] A. Örnek, E. Bulut, M. Can, M. Özacar, Characteristics of nanosized LiNi x Fe1−x PO_4/C (x = 0.00–0.20) composite material prepared via sol–gel-assisted carbothermal reduction method, Journal of Solid State Electrochemistry 17 (2013) 3101–3107. https://doi.org/10.1007/s10008-013-2201-5.

Acknowledgments

The authors highly acknowledge the financial support from the (i) ARCI-Technical Research Center {Ref. No. AI/1/65/ARCI/2014 (c)} funded by the Department of Science and Technology (DST), Government of India, (ii) IRHPA Project (Ref. No. IPA/2021/000007) funded by Science and Engineering Research Board (iii) DST-ICMAP (Ref.No.DST/TMD/IC-MAP/2K20/01/C) funded by the Department of Science and Technology (DST), Government of India, (iv) AMEST Project (Ref. No. DST/CEST/AMEST/2022/57 (C)/2) funded by Department of Science and Technology (DST), Government of India.

Conflicts of interest

The authors have no conflicts to declare.

Declaration of interests

☒The authors declare that they have no known competing financial interests or personal relationships that could have appeared to influence the work reported in this paper.

☐The authors declare the following financial interests/personal relationships which may be considered as potential competing interests:

Graphical Abstract

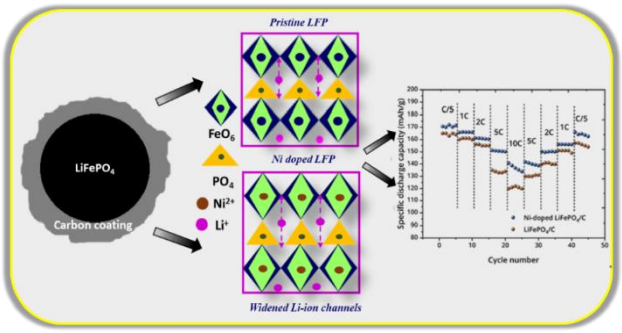

Highlights

- High-rate performance Ni doped $LiFePO_4$ was prepared by scalable solid-state route.
- Widened Li-O bonds showed better diffusion kinetics for Ni-LFP/C than pristine LFP.
- Effect of Ni doping on LFP crystal structure was analyzed using DFT calculations.
- Ni-LFP delivers high-rate capability with specific capacity of 136 mAh/g at 10C.